



Cite this: *Energy Environ. Sci.*, 2018, 11, 2372

Received 15th May 2018,
Accepted 21st June 2018

DOI: 10.1039/c8ee01377b

rsc.li/ees

Stringed “tube on cube” nanohybrids as compact cathode matrix for high-loading and lean-electrolyte lithium–sulfur batteries†

Gaoran Li,^{‡,a} Wen Lei,^{‡,b} Dan Luo,^{Ⓜ^a} Yaping Deng,^a Zhiping Deng,^b Deli Wang,^{Ⓜ^{*b}} Aiping Yu,^{Ⓜ^a} and Zhongwei Chen,^{Ⓜ^{*a}}

The rational design of cathode host materials is significant in fulfilling high-efficiency sulfur electrochemistry as well as boosting the energy density of lithium–sulfur (Li–S) batteries. Herein, we develop a stringed “tube on cube” nanohybrid (CPZC) with a ternary hierarchical architecture, which contains a fibrous carbon skeleton, highly porous carbon cube filler, and abundant CNT tentacles as an advanced matrix for sulfur electrodes. The as-developed CPZC delivers excellent conductivity, abundant active interfaces, and strong confinement to polysulfide, and thus is capable of significantly expediting the sulfur redox kinetics and promoting battery durability. The fabricated sulfur electrode achieves a superb rate capability up to 10C, outstanding cyclability over 2000 cycles, and more importantly, excellent performance under high a sulfur loading and sparing electrolyte with a high energy density of 348.8 W h kg^{−1} and 327.6 W h L^{−1} at the system level, which reveals its potential in promoting the practical application of Li–S batteries.

Broader context

Lithium–sulfur (Li–S) batteries represent one of the most promising battery chemistries beyond the currently dominating Li-ion technology to support the ever-expanding electrical market. However, the practical implementation of Li–S batteries is still impeded by several intractable obstacles including the insulating nature of active sulfur, the shuttling behaviour of intermediate polysulfides, and the volume variation during battery operation. Thus, the rational design of cathode structure serves as a crucial pathway toward practically viable Li–S batteries. Herein, we report the target-oriented design of a hierarchical conductive fabric (CPZC) as an advanced self-standing cathode matrix for enhanced Li–S battery performance. This elaborate structure endows the as-developed CPZC with excellent charge transfer, robust electrode integrity, and strong sulfur confinement, thus enabling intriguingly fast and durable sulfur electrochemistry even under a high sulfur loading and low electrolyte. This work offers an instructive paradigm of rational material engineering to address the aforementioned challenges and promote the electrochemical performances of Li–S batteries.

Introduction

Since conventional lithium-ion batteries (LIBs) are approaching their theoretical limits, the development of battery chemistry beyond the lithium-ion intercalation mechanism is necessary to meet the ever-growing energy demand. Among the candidates, lithium–sulfur (Li–S) batteries exhibit great promise to revolutionize the energy storage field due to their high energy density, which is theoretically quintuple that of conventional LIBs (2500 vs. 500 W h kg^{−1}).^{1–3} Besides, the cost effectiveness and

good environmental benignity of Li–S batteries further strengthen their prospect for high-efficiency and sustainable energy storage.^{4,5} However, the practical implementation of Li–S batteries is still retarded by several obstacles including the insulating nature of elemental sulfur and its lithiation products, the dissolution and shuttling behaviors of the intermediate polysulfides, and the large volume variation of active materials during the battery cycling, which result in unsatisfactory practical energy densities and poor operational durability.⁶

During the past few decades, numerous research efforts have been dedicated to address these problems, which include but are not limited to, multifarious cathode structures, functional interlayers, electrolyte modifications, and anode protections.^{7–9} Among them, the rational construction of the sulfur cathode plays a particularly important role in fulfilling high-efficiency sulfur electrochemistry and boosting the battery performance. The rationale behind the design of sulfur electrodes relies on several principles considering the unique characteristics

^a Department of Chemical Engineering, Waterloo Institute for Nanotechnology, Waterloo Institute for Sustainable Energy, University of Waterloo, Waterloo, Ontario N2L 3G1, Canada. E-mail: zhwen@uwaterloo.ca

^b Key Laboratory of Material Chemistry for Energy Conversion and Storage, Hubei Key Laboratory of Material Chemistry and Service Failure, School of Chemistry and Chemical Engineering, Huazhong University of Science and Technology, Wuhan 430074, P. R. China. E-mail: wangdl81125@hust.edu.cn

† Electronic supplementary information (ESI) available. See DOI: 10.1039/c8ee01377b

‡ These authors contribute equally to this work.

of Li-S electrochemistry: (i) the deficiency of both ionic and electrical insulations for the active materials requires the establishment of a pass-through system that allows rapid electron and ion conduction within the cathode for sufficient sulfur redox reactions. Additionally, it is worth noting that the conventional fabrication of sulfur electrodes is generally based on particle-type materials and slurry-casting technology, where the indispensable utilization of non/poorly conductive polymer binder not only deteriorates the charge transfer within the electrode, but also easily induces the loss of conductive contact between the particles when sulfur species dissolve in the electrolyte. This leads to sluggish reaction kinetics as well as vulnerable electrode integrity.¹⁰ Accordingly, a binder-free, highly interconnected, and uninterrupted conductive matrix holds great promise to support good electrode robustness and favorable long-range electrical conductivity.^{11,12} (ii) In addition, sulfur electrochemistry in the liquid configuration strongly relies on the phase conversions between solid and liquid sulfur species on the electrode surface. Accordingly, this calls for abundant electrode/electrolyte interfaces for sufficient sulfur redox reactions.¹³ (iii) Besides, the intrinsically high solubility and mobility of the intermediate polysulfides in the electrolyte give rise to severe sulfur loss and detrimental anodic reactions. Hence, a well-designed electrode structure is also expected to effectively confine the sulfur species within the cathode to inhibit the shuttling effect and enhance the energy efficiency.^{14,15} (iv) Furthermore, the energy density of the Li-S battery system relies on the synergism between the electrodes and electrolyte. An insufficient sulfur loading and excessive usage of electrolyte severely compromise the energy density at the system level and easily fail to meet the demands of practical applications.^{16,17} Therefore, the sulfur electrode is also required to be rationally designed and capable of sustaining decent sulfur electrochemistry under a considerably high sulfur loading and a minimal electrolyte dosage for a practical viable energy density at the system level.

Thus, considering these rules, we elaborately develop a stringed “tube on cube” carbonaceous hybrid (denoted as CPZC) with a ternary hierarchical architecture consisting of a fibrous skeleton, porous cubic fillers, and carbon nanotube (CNT) tentacles rooted on the cubes as an advanced sulfur host for enhanced Li-S battery performance. During its synthesis, the polyacrylonitrile (PAN)-derived carbon impregnates the

ZIF-67-derived carbon cubes within the fibrous skeleton, while the CNTs are grown *via* a sequential CVD process to further interlink the fibers and form a self-standing and highly conductive network. The as-developed hierarchical architecture delivers a highly interconnected fibrous network for long-range and fast electron conduction, high porosity for easy electrolyte infiltration and rapid ion transfer, as well as high surface area for sufficient interfacial reactions, thus allowing efficient and fast sulfur redox reactions. Meanwhile, the high porosity and intrinsic element doping in CPZC result in strong physical and chemical confinements to polysulfides, which contribute to the effective inhibition of shuttling behavior and enhancement in battery durability. Consequently, the as-developed CPZC realizes an excellent electrochemical performance, *i.e.*, high rate capability up to 10C and outstanding cyclability with an ultra-low capacity fading rate of 0.016% per cycle over an ultralong test of up to 2000 cycles. More importantly, these unique structural advantages enable excellent battery electrochemistry under practical conditions, namely a high sulfur loading of up to 13.5 mg cm⁻² and lean electrolyte usage as low as $E/S = 3 \text{ mL g}^{-1}$, with an attainable energy density of 348.8 W h kg⁻¹ and 327.6 W h L⁻¹ at the system level, which demonstrate intriguing potential for practical applications.

Results and discussion

Fig. 1 illustrates the synthetic process of the CPZC fabric (see details in the Experimental section, ESI†). The zeolitic imidazolate framework-67 (ZIF-67) nanocubes with a uniform size were prepared first, as previously reported (Fig. S1, ESI†).¹⁸ The XRD pattern of ZIF-67 confirms its crystallinity, which displays the characteristic sharp peaks consistent with previous reports (Fig. S2, ESI†).¹⁹ Subsequently, the obtained ZIF-67 nanocubes were uniformly dispersed in PAN/DMF solution with a PAN to ZIF-67 weight ratio of 2:1, which was then employed for electrospinning to prepare the self-standing composite fabric thin film. For comparison, the pure PAN fabric was also prepared under the same conditions using the blank PAN/DMF solution as the electrospinning precursor. The obtained

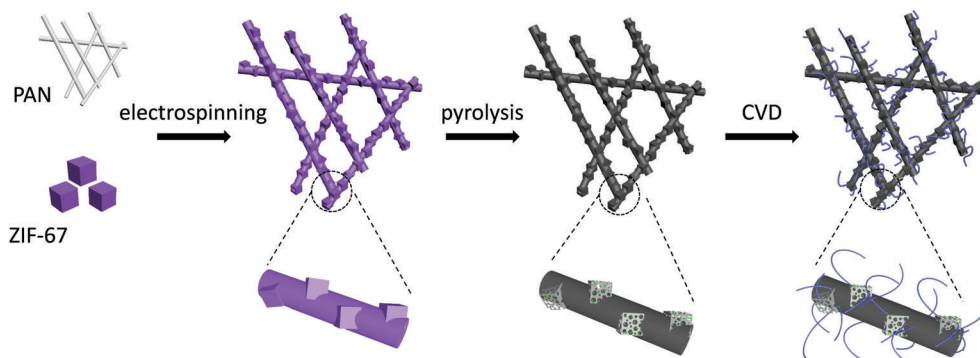


Fig. 1 Schematic illustration of the synthesis of the CPZC fabric.

PAN@ZIF composite (PZ) film was purple color, in contrast to the white pure PAN film, as shown in Fig. S3, ESI†. The SEM results reveal a smooth surface for the pure PAN fiber, whereas the obtained PZ composite fiber clearly exhibits cubic particles impregnated within the PAN skeleton and a simultaneously increased fiber diameter (Fig. S4, ESI†). The XRD pattern confirms the successful impregnation of ZIF-67 in the PAN matrix with sharp peaks indexed to the ZIF crystallite in the PZ composite fiber (Fig. S5, ESI†). PZ composite fibers with different PAN to ZIF ratios (10:1, 5:1, and 3:1) were also prepared, as shown in Fig. S6, ESI†. The morphology variation involving an increase in the quantity of cubes and widening of the fiber diameter can be clearly observed with an increase in the PAN to ZIF ratio. However, a higher ZIF dosage (>2:1 for PAN to ZIF ratio) failed to maintain the encapsulation structure, thus 2:1 was employed as the optimized ratio. Afterwards, the obtained PZ fiber was pyrolyzed under an argon atmosphere to yield the carbonaceous composite fiber (denoted as CPZ). After pyrolysis, the carbonized PAN (CP) fiber retained a smooth surface and solid fibrous morphology (Fig. 2a–c). By contrast, the PZ sample was transformed into a binary hierarchical architecture hybridizing the fibrous skeleton and highly porous cubic filler (Fig. 2d–f), where the ZIF-derived porous carbon cubes embedded with abundant cobalt nanoparticles were uniformly stringed by the PAN-derived fiber matrix. Accordingly, CPZ samples based on different PAN to ZIF ratios were also prepared. The SEM and TEM images show the good encapsulation structure in all the fabrics, while a significant increase in the quantity of the cubic filler and porosity of the composite fabric can be observed with an increase

in the dosage of ZIF in the precursor (Fig. S7, ESI†). When applied as a sulfur host, the highly porous carbon cube filler is expected to offer effective nanoconfinement and uniform distribution for active sulfur to ensure fast short-range electron conduction, while the tight packing by the long length-diameter fibrous carbon promises good long-range conductivity. Accordingly, the obtained CPZ was subjected chemical vapor deposition (CVD) treatment to construct accessible carbon nanotubes rooted on the CPZ substrate. The obtained PAN@ZIF@CNT composite fabric (denoted as CPZC) was endowed with a ternary hierarchical architecture with a CP fibrous skeleton, porous hollow carbon cube fillers, and CNT tentacles, as observed in Fig. 2g–i. The CNT amount in the obtained CPZC composite fabric continued to increase with an increase in the amount of ethylenediamine, as shown in Fig. S8, ESI†. As the CNT content tended to saturation with a further increase in the gas source, 3 mL ethylenediamine was adopted as the optimized value for CNT construction (Fig. S9, ESI†). The grown CNTs have a width of dozens of nanometers and length of several micrometers with a bamboo-like morphology constructed by highly graphitic walls (Fig. 2h and i and Fig. S10, ESI†). More importantly, the CNTs intertwine in the junctions between adjacent fibers, which contributes to the strengthened structural integrity and facilitates electron conduction within the entire matrix (Fig. S11, ESI†).

The structural characters of the as-developed carbonaceous products were investigated *via* XRD measurements (Fig. 3a). Different from the pure CP sample, which shows a typical XRD pattern indexed to amorphous carbon, sharp peaks corresponding to the metallic cobalt can be clearly observed for both

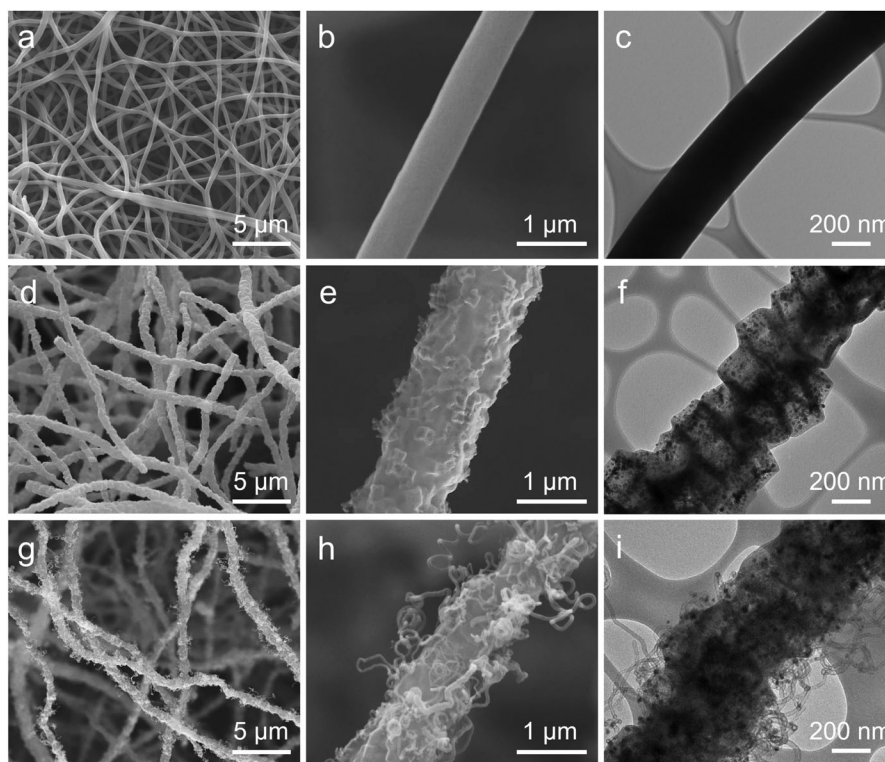


Fig. 2 Morphological characterization. SEM and TEM images of the obtained (a–c) CP, (d–f) CPZ, and (g–i) CPZC fibers.

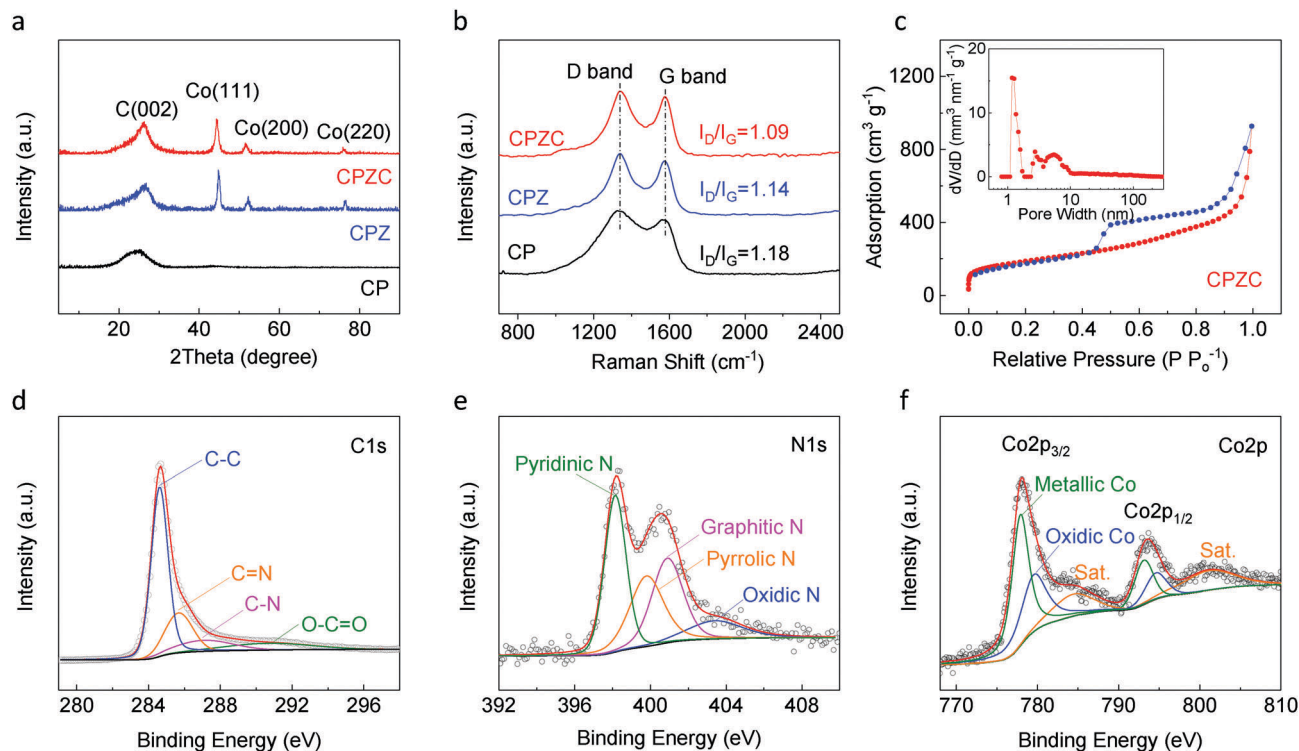


Fig. 3 Structural characterization. (a) XRD patterns and (b) Raman spectra of the CP, CPZ, and CPZC fabrics. (c) N_2 adsorption/desorption isotherm curve and pore distribution (inset) of the CPZC composite fabric. High-resolution XPS spectra of (d) C1s, (e) N1s, and (f) Co2p for the CPZC composite fabric.

the CPZ and CPZC samples, confirming the existence of Co nanoparticles in their carbon matrix. This result is also consistent with the above morphology observations. Notably, CPZ and CPZC show sharper peaks at around 25° than that in the CP pattern, which corresponds to the (002) lattice plane of carbon and implies higher graphitization in CPZ and CPZC contributed by the catalytic actions of the metal cobalt nanoparticles.^{20,21} This result is further supported by their Raman spectra, as shown in Fig. 3b. Two peaks located at 1342 and 1578 cm^{-1} can be observed in the Raman spectra of all these samples, which correspond to the disorder-induced vibrational mode in the hybridized carbon rings (D band) and the symmetry-allowed vibrational feature of the sp^2 carbon atom pairs (G band), respectively.^{22,23} The intensity ratio of the D band to G band (I_D/I_G) is a well-acknowledged indicator negatively correlating the degree of carbon graphitization.²⁴ Accordingly, a decrease in the degree of disorder in the sp^2 carbon lattice can be observed going from CP to CPZ and CPZC, which is attributed to the catalyzed graphitization by the metal Co sites during the pyrolysis process, as mentioned above. The improved graphitization is also confirmed by the high-resolution TEM study, where abundant lattice fringes of graphitized carbon can be clearly observed (Fig. S12, ESI†). The lowest I_D/I_G ratio was obtained for the CPZC sample owing to the additional contribution by the highly graphitized carbon walls in the CNTs (Fig. S10, ESI†). These results consistently confirm the high degree of graphitization of the as-developed CPZC, which has the potential to offer favorable electron conduction. Due to the synergetic combination of the interconnected fibrous skeleton,

highly graphitized carbon structure, and CNT intertwined fiber junctions, CPZC exhibits the highest conductivity of 11.5 S cm^{-1} among the obtained samples (Fig. S13, ESI†), which holds great promise for fast sulfur redox reactions.

The pore structures of the as-developed samples were investigated *via* N_2 adsorption-desorption analysis (Fig. 3c and Fig. S14, ESI†). The comparison of their isotherms displays a significant enhancement in porosity from CP to CPZ (Fig. S14a and c, ESI†), which is consistent with the morphology variation observed in Fig. 2. CPZ exhibits a much higher BET surface area of $743.5\text{ m}^2\text{ g}^{-1}$ and pore volume of $1.55\text{ cm}^3\text{ g}^{-1}$ than that of CP ($34.2\text{ m}^2\text{ g}^{-1}$ and $0.023\text{ cm}^3\text{ g}^{-1}$, respectively). Furthermore, a significant enhancement in both micro- and meso-porous structure can be observed from CP to CPZ (Fig. S14b and d, ESI†), which is attributed to the fact that the decomposition of the ZIF-67 particles not only transforms them into highly porous hollow carbon nanocubes, but also induces pore formation in the PAN substrate through the impact, corrosion, and activation by the decomposition products.²⁵ Additionally, the interaction between the CNTs causes a slight loss in porosity from CPZ to CPZC ($665.6\text{ m}^2\text{ g}^{-1}$ and $1.45\text{ cm}^3\text{ g}^{-1}$, respectively) but with an increase in the proportion of meso/macro-pores, which is attributed to the intrinsic pore characteristics of the CNTs (Fig. 3c and Fig. S14c and d, ESI†).²⁶ The high porosity of CPZC is expected to offer strong physical confinement to sulfur species for inhibited shuttling behavior, while its high surface area introduces abundant electrode/electrolyte interfaces easily accessible to both electrons and ions for fast and efficient sulfur interfacial

reactions. Moreover, its high pore volume is also promising to enable a high-efficiency sulfur loading, electrolyte infiltration, and good accommodation to the volume variation upon battery cycling. Therefore, the as-developed CPZC delivers an intriguing porous structure to favor fast and durable sulfur electrochemistry.

The surface chemistry of the as-developed CPZC was studied *via* XPS. The survey spectrum confirms the existence of nitrogen and cobalt in CPZC, which have characteristic peaks at around 400 and 780 eV, respectively (Fig. S15, ESI†). The high-resolution C1s spectrum of CPZC shows four subpeaks, where the two located at 285.7 and 287.2 eV are assigned to the C=N and C-N bonds, respectively, which verify the heteroatom doping of N in the carbon matrix (Fig. 3d).^{27,28} The N-doping originated from the decomposition of both PAN and the organic ligands in the ZIF-67 crystal, while the CNTs derived from ethylenediamine also contribute to additional N sites, as evidenced by the element mapping results (Fig. S16, ESI†). The N and Co contents in the as-developed CPZC fabric are around 7.8 and 13.1 wt%, respectively, according to the EDX and combustion analysis. The chemical status of the dopant N was further revealed by the high-resolution N2p spectra, as shown in Fig. 3e. The spectrum can be differentiated into four subpeaks corresponding to pyridinic N (398.2 eV), pyrrolic N (399.8 eV), graphitic N (400.9 eV), and oxidic N (403.5 eV). In addition, the high-resolution Co2p spectra of CPZC show peaks assigned to Co2p_{3/2} and Co2p_{1/2} at 778.1 and 793.6 eV, respectively. The deconvoluted spectra exhibit metallic Co, oxidic Co and satellites, as depicted in Fig. 3f.^{20,29} The XPS results manifest that the as-developed CPZC is enriched with N doping and Co species. The doping chemistry is expected to favor the sulfur redox reactions by endowing the carbon substrate with a more polar surface, which can effectively immobilize polysulfides *via* chemical adsorption to inhibit polysulfide shuttling and improve battery durability. The chemical interactions between polysulfide and CPZC were verified by further XPS analysis. As shown in Fig. S17a, ESI†, the S2p spectrum of pristine Li₂S₆ shows typically two pairs of peaks at 161.3 and 162.8 eV, which correspond to the terminal sulfur (S_T) and bridging sulfur (S_B), respectively.³⁰ After it is adsorbed by CPZC, a significant shift can be observed for these peaks to a higher energy range, which suggests a decrease in the electron cloud density in the sulfur atoms as a result of the chemical bonding between Li and N to form a “lithium bond” interaction.^{31,32} In addition, two pairs of new peaks corresponding to the sulfite and sulfate species emerge in the high binding energy range, which signify the interactions between polysulfide and oxidic species in CPZC.³³ Notably, a new peak appears at a low binding energy of 160.4 eV, which corresponds to the Co-S bonding and indicates the chemical interactions between polysulfide and the Co sites. Besides, the Li1s spectra also display a broadened peak and the emergence of a new subpeak ascribed to the Li-N bonding, which is consistent with the above results (Fig. S17b, ESI†).³⁴ All these results collectively verify the strong chemical interactions between CPZC and polysulfide, which are expected to chemically strengthen the sulfur immobilization in Li-S batteries.

Furthermore, the interactions between CPZC and polysulfide were also simulated and inspected through a visual adsorption

measurement. Initially, an Li₂S₆ solution was prepared by stoichiometrically dissolving elemental sulfur and lithium sulfide in dimethoxy ethane/1,3-dioxolane (DME/DOL) binary solvent. Then, CP, CPZ, and CPZC were immersed into the solution as polysulfide absorbers for 24 h. As shown in Fig. S18, ESI† the blank Li₂S₆ solution was light brown in color. However, after adsorption by CPZC, the solution became almost colorless and transparent, indicating its superb capability of adsorbing polysulfide. This result is also confirmed by the UV-vis analysis. The UV-vis spectrum of the blank Li₂S₆ solution shows two peaks located at around 411 nm and 280 nm, which are assigned to the S₆²⁻ and S₄²⁻ species, respectively.^{35,36} Comparatively, the solution adsorbed by CPZC exhibits a much more drastic intensity decrease for these peaks compared to that for CP and CPZ, which indicates the significant decrease in polysulfide concentration in solution and admirable polysulfide adsorption capability of the as-developed CPZC. The superior polysulfide adsorption of CPZC is attributed to two factors: (a) the strong chemical interactions between polysulfide and CPZC serve as effective traps to anchor the polysulfide species on its surface and (b) the high porosity of CPZC provides favorable physical confinement to polysulfide, while simultaneously, its high surface area exposes more active sites for both physical and chemical adsorption.

Considering these structural and chemical superiorities, CPZC was then applied as the sulfur host material to investigate its practical improvement in battery performance. A sulfur-CPZC composite (S@CPZC) was prepared *via* the conventional melt-diffusion method (see details in the Experimental section, ESI†), and used as the sulfur electrode directly for electrochemical characterization. Sulfur composite electrodes based on CP and CPZ (denoted as S@CP and S@CPZ, respectively) were also prepared for comparison. The XRD pattern verifies the successful loading of sulfur in the composite, which shows sharp peaks indexed to orthorhombic sulfur (PDF#08-0247, Fig. S19, ESI†). The significantly weakened adsorption/desorption behavior, as shown in the isotherm curve after sulfur loading, indicates efficient sulfur occupation in the CPZC pores (Fig. S20, ESI†). Moreover, the element mapping also demonstrates the uniform sulfur distribution in the obtained composite (Fig. S21, ESI†). These results manifest the successful and uniform sulfur loading in the obtained sulfur composite. The sulfur content in the composite was determined to be 75.2 wt% by TGA analysis (Fig. S22, ESI†). The conductivities of the sulfur composites were also investigated, as shown in Fig. S13, ESI†. It should be noted that the conductivity of the obtained sulfur composite depends on not only the intrinsic electron conduction property of the host material, but also the sulfur distribution status within its matrix. Benefiting from the high porosity and large surface area of CPZC, sulfur can be well dispersed on the conductive surface, thus contributing to the highest composite conductivity as well as the smallest conduction fading after sulfur loading compared with that of CP and CPZ. This result further illustrates the great structural superiorities of the as-developed CPZC as sulfur host material.

The electrochemical evaluation of the obtained sulfur electrodes was initially performed by galvanostatic charge-discharge tests.

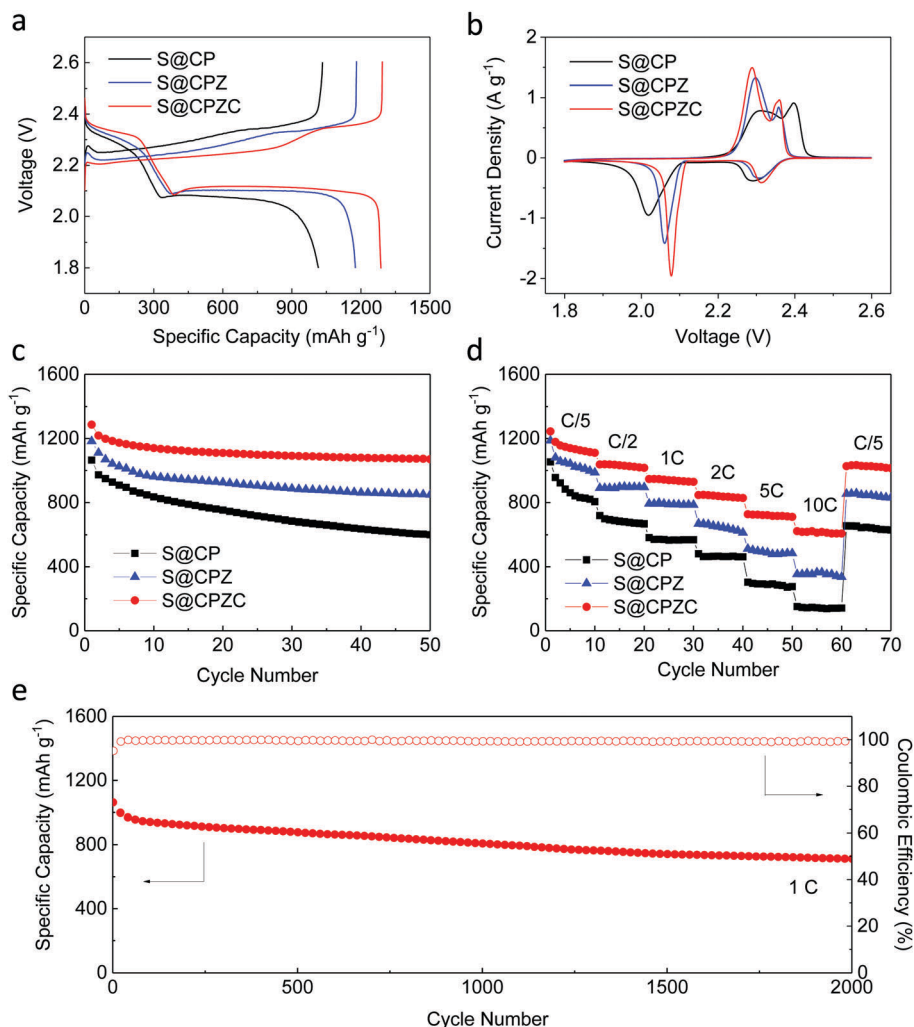


Fig. 4 Electrochemical characterization. (a) Voltage profiles at a rate of C/5, (b) CV curves at 0.1 mV s^{-1} , (c) cycling performances at a rate of C/5, and (d) rate performances of different sulfur electrodes based on CP, CPZ, and CPZC. (e) Long-term cycling performance of the S@CPZC electrode at a rate of 1C.

Fig. 4a shows the typical voltage profiles of the different sulfur electrodes at a rate of C/5 ($1\text{C} = 1675 \text{ mA g}^{-1}$). All the electrodes exhibit the typical two-plateau discharge curves, which correspond to the multi-step sulfur electro-reduction. The higher discharge plateau located at around 2.3 V (vs. Li^+/Li , hereinafter inclusive) corresponds to the transformation from solid elemental sulfur to high-ordered polysulfides (Li_2S_n , $4 < n \leq 8$), which dissolve in the ether-based electrolyte. The further reduction of polysulfides to form low-ordered and insoluble Li_2S_2 and Li_2S contributes to the lower discharge plateau at around 2.1 V. The cell charging undergoes a reverse process by showing two corresponding charge plateaus. The cyclic voltammetry (CV) curves are consistent with the voltage profiles, which show two pairs of sulfur redox peaks within the studied potential range (Fig. 4b). It is worth noting that the S@CPZC electrode delivers a high initial specific capacity of $1286.9 \text{ mA h g}^{-1}$, which is 76.8% of its theoretical limit and much higher than that of the S@CP ($1015.3 \text{ mA h g}^{-1}$) and S@CPZ ($1175.7 \text{ mA h g}^{-1}$) electrodes, indicating enhanced sulfur utilization in the S@CPZC

electrode. This is attributed to the high conductivity and large surface area of CPZC, which offer abundant electrode/electrolyte interfaces easily accessible to electrons and ions for thorough sulfur redox reactions. Additionally, the S@CPZC electrode also shows the smallest potential gap between the charge and discharge plateaus among the three electrodes, while its CV curve consistently delivers the sharpest peaks and smallest redox potential gaps (Fig. S23, ESI[†]). These results strongly indicate the facilitated sulfur redox reactions and fast kinetics for the CPZC-based sulfur electrode. Fig. 4c shows the cycling performances of the different sulfur electrodes. It can be clearly observed that S@CPZC electrode delivers the highest capacity and best cycling stability among the sulfur electrodes with a high capacity retention of 82.4% ($1059.8 \text{ mA h g}^{-1}$) after 50 cycles at a rate of C/5 rate, while the S@CPZ and S@CP electrodes retain only 72.7% ($848.7 \text{ mA h g}^{-1}$) and 59.1% ($600.15 \text{ mA h g}^{-1}$) of their initial capacities, respectively. Additionally, the cycling performances of the S@CPZ electrodes with different PAN to ZIF ratios and S@CPZC electrodes with different CNT contents were also

investigated, as shown in Fig. S24 and S25, ESI†. A clear evolution of the enhanced cyclability for the corresponding sulfur electrodes can be observed with an increase in the PAN to ZIF ratio and the CNT content, which further confirms the great benefits of these structures for durable sulfur electrochemistry. The superior cyclability of the S@CPZC electrode is attributed to the strong sulfur confinement *via* the combined physical and chemical interactions between CPZC and polysulfide, as verified above, which efficiently immobilize the active sulfur within the cathode and suppress polysulfide shuttling, leading to stable battery cycling behavior. Furthermore, post-cycling morphological characterization was performed to investigate the structural stability of the as-developed CPZC upon battery cycling. As shown in Fig. S26a, ESI†, the S@CPZC electrode disassembled from a cycled cell well maintained the fibrous architecture. After washing with THF and CS₂ to remove the sulfur species, a clearer hierarchical stringed “tube on cube” hybrid structure can be observed, as shown in Fig. S26b and c, ESI†, which strongly illustrates the excellent structural stability of CPZC upon battery cycling.

The rate capabilities of the obtained sulfur electrodes were evaluated through multi-rate cycling, as shown in Fig. 4d. The S@CPZC electrode retains an intriguingly high capacity of 622.6 mA h g⁻¹ at a high current rate of up to 10C, which recovers to 1032.3 mA h g⁻¹ as the current is reduced back to a rate of C/5, indicating its fast sulfur redox kinetics and highly reversible electrochemistry. This result is consistent with the smallest polarization in the voltage profiles and CV curves, as previously discussed, as well as the smallest internal resistance in the EIS spectra (Fig. S27, ESI†). In contrast, the S@CPZ and S@CP electrodes show much poorer rate capabilities with low capacities of 364.4 mA h g⁻¹ and 145.9 mA h g⁻¹, respectively, at a rate of 10C. The superior reaction kinetics of the S@CPZC electrode benefits from its high electrical conductivity and high surface area with abundant electrode/electrolyte interfaces for fast electron/ion transfer. Meanwhile, its strong adsorption of polysulfides also establishes a high-concentration layer of active sulfur species, which in turn favors fast sulfur redox reactions. The improved reaction kinetics of the S@CPZC electrode was further verified by CV measurements in a symmetrical coin cell configuration. As shown in Fig. S28, ESI†, the symmetrical Li₂S₆-Li₂S₆ cell based on CPZC exhibits a much higher current density than that with CP and CPZ, which indicates its great capability of fulfilling fast and sufficient electrochemical polysulfide reactions.³⁷ Accordingly, the S@CPZC electrode was subjected to a long-term galvanostatic cycling test, as shown in Fig. 4e. The as-developed S@CPZC electrode achieved outstanding cyclability with an ultralow capacity fading rate of 0.016% per cycle and a constantly high coulombic efficiency exceeding 99% over the ultra-long 2000 cycles at a rate of 1C. It should be noted that the cyclability and rate capability demonstrated in this work is highly competitive among the recently published literature based on fibrous sulfur electrodes (Table S1, ESI†) and other host materials with various morphologies (Table S2, ESI†), which further supports the great structural superiorities of CPZC in boosting the sulfur reaction kinetics and prolonging the battery lifespan.

As a promising alternative energy storage technology to the currently dominant Li-ion batteries, the development of Li-S batteries is required to focus more on the practical performance at the system level rather than specific evaluation solely on the sulfur electrode. Despite the encouraging progress made in the past few decades, most of the good performances are achieved under a low areal sulfur loading (<1.5 mg cm⁻²) and high electrolyte content ($E/S > 10$ mL g⁻¹, E/S represents the electrolyte to sulfur ratio).³⁸ On the one hand, cathodes with a low sulfur loading can hardly achieve competitive areal capacities with the state-of-art Li-ion batteries, while the abuse of electrolyte further compromises the energy density of Li-S batteries both gravimetrically and volumetrically at the system level. On the other hand, the above-mentioned problems of sulfur electrochemistry become more intractable under a considerably increased sulfur loading and sparing electrolyte usage.^{39,40} Therefore, a rationally designed cathode structure is desirable to support decent sulfur electrochemistry under these conditions to give a viable energy density for Li-S batteries. Accordingly, the as-developed S@CPZC electrode was further employed to pursue a high sulfur loading and low electrolyte content to explore its potential for practical use. Thicker electrodes were prepared for an increased sulfur loading to maintain the sulfur content at around 75 wt% in the composites (Fig. S29, ESI†). As shown in Fig. 5a, the S@CPZC electrodes exhibit a continuous increase in areal capacity with the enhancement in areal sulfur loading. A reversible areal capacity of 4.66 mA h cm⁻² was achieved at a sulfur loading of 5.1 mg cm⁻², which outperforms that of the commercial Li-ion battery (typically 3.0–4.0 mA h cm⁻²) and implies its good promise in yielding a competitively high energy density.^{41,42} As the sulfur loading was further increased to 9.2 mg cm⁻², an even higher areal capacity of up to 8.2 mA h cm⁻² was achieved despite the slight deterioration in cycling stability to a certain extent. It should be noted that although a high areal capacity can be obtained upon increasing the sulfur loading, the specific capacity continues to fade with this variation. This signifies the limited sulfur utilization resulting from the impeded electron and ion transfer within the thick electrode (Fig. S30, ESI†). Besides, deteriorated cycling stability was also observed particularly for the electrodes with an ultra-high sulfur loading (≥ 9.2 mg cm⁻²), which is ascribed to the considerably concentrated polysulfides and their aggravated shuttling behaviour, which lead to not only high viscosity of the electrolyte and poor ion transfer, but also serious corrosion on the lithium surface. In addition to the sulfur loading, the electrolyte dosage was also optimized to achieve a high energy density at the system level. It can be observed that the voltage profiles of the S@CPZC electrode (sulfur loading: 5.1 mg cm⁻²) displayed reduced capacities and aggravated polarization with a decrease in the E/S ratio from 12 to 3 mL g⁻¹, which implies the deterioration of sulfur utilization and sulfur redox kinetics (Fig. 5b and Fig. S31a, ESI†). The decrease in electrolyte induces insufficient wetting of the electrode surface, and thus fails to offer adequate electrolyte/electrode interfaces for thorough sulfur conversion reactions. In addition, the lack of electrolyte also gives rise to a high polysulfide concentration and electrolyte viscosity upon the

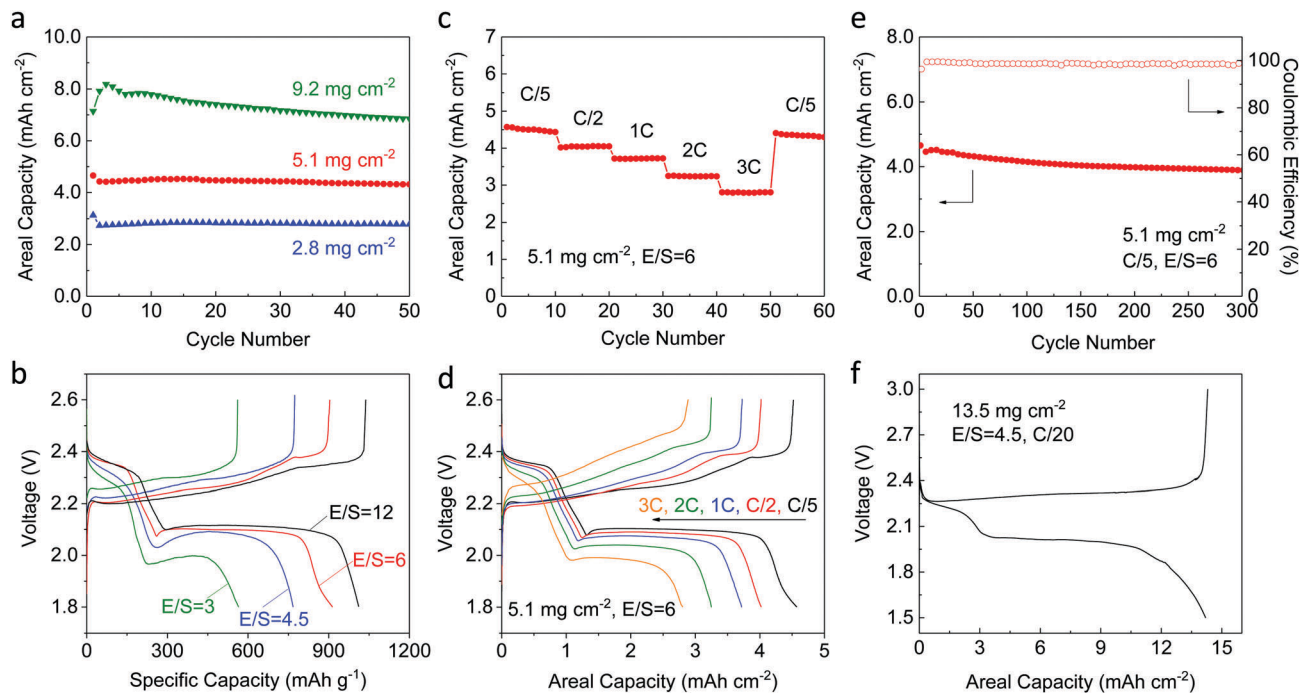


Fig. 5 High-loading and lean-electrolyte performances of the S@CPZC electrodes. (a) Cycling performances of the S@CPZC electrodes with an increased sulfur loading at a rate of C/5. (b) Voltage profiles of the S@CPZC electrodes with different E/S ratios at a rate of C/5. (c) Rate performance, (d) multi-rate voltage profiles, and (e) long-term cycling performance at a rate of C/5 for the S@CPZC electrodes under a sulfur loading of 5.1 mg cm^{-2} and E/S ratio of 6. (f) Voltage profile of the S@CPZC electrode under an extremely high sulfur loading of 13.5 mg cm^{-2} and low E/S ratio of 4.5 at a rate of C/20.

sulfur electrochemical reactions, leading to severely impeded ion transportation and increased electrochemical impedance (Fig. S31b, ESI[†]). Nevertheless, a clear two-plateau discharge profile was still achieved even at an extremely low E/S ratio of 3 (Fig. 5b), which indicates the great structural superiority of CPZC in maintaining good sulfur electrochemistry under a low electrolyte content.

Based on these results, the optimized sulfur loading of 5.1 mg cm^{-2} and E/S ratio of 6 mL g^{-1} were employed to investigate the rate capability and cycling stability of the S@CPZC electrode under a high loading and low electrolyte configuration. As shown in Fig. 5c, a decent areal capacity of 2.8 mA h cm^{-2} was retained for the S@CPZC electrode at a high current rate of up to 3C, which recovered to 4.4 mA h cm^{-2} when the current rate was adjusted back to C/5, indicating the fast and reliable sulfur electrochemistry even under these more practical conditions. Fig. 5d shows the voltage profiles of the S@CPZC electrode at different current rates. The potential gaps between the charge and discharge curves are observed to expand with an increase in current rate. Nevertheless, a distinct two-plateau charge–discharge profile was still obtained at high rate of 3C, which further confirms the superiority of the CPZC matrix in fulfilling fast sulfur redox reaction kinetics. In addition, long-term galvanostatic cycling was also performed for the S@CPZC electrode under these conditions. The results show the excellent cycling stability of the S@CPZC electrode with a high capacity retention of 3.9 mA h cm^{-2} even after 300 cycles, which indicates its admirable capability of inhibiting polysulfide shuttling and promoting durable sulfur electrochemistry under practical conditions (Fig. 5e). Furthermore, an extreme attempt using

the S@CPZC electrode with an ultra-high sulfur loading of 13.5 mg cm^{-2} and sparing electrolyte of 4.5 mL g^{-1} was performed to challenge the attainably high energy density. An expanded voltage window and lower current rate were applied to draw more energy. As shown in Fig. 5f, the as-developed S@CPZC electrode fulfils an ultra-high areal capacity of $14.2 \text{ mA h cm}^{-2}$ with a typical two-plateau discharge curve, indicating the great superiority of CPZC in maintaining decent sulfur electrochemistry even under these harsh conditions. However, considerable electrochemical polarization in the voltage profile and limited capacity retention during the cycling were observed, which indicate obstructed sulfur redox reactions to a certain extent (Fig. S32, ESI[†]). More importantly, high gravimetric and volumetric energy densities ($348.8 \text{ W h kg}^{-1}$ and 327.6 W h L^{-1} , respectively) at the system level (covering the mass/volume of the cathode, electrolyte, and anode) were achieved for the S@CPZC-based Li-S battery, which is highly promising to outperform the conventional Li-ion batteries gravimetrically (around 170 W h kg^{-1}), and also highly competitive among the recently reported Li-S configurations based on high-loading fibrous electrodes (Fig. S33 and Table S3, ESI[†]). All these results manifest the great potential of the as-developed CPZC in pursuing high-energy-density and long-life Li-S batteries for future energy storage applications.

Conclusions

In conclusion, we developed a stringed “cube on tube” nano-hybrid as an advanced sulfur host for high-performance Li-S

batteries. In this elaborate hierarchical architecture, the ZIF-67-derived carbon cube fillers are highly porous with abundant N and Co sites, which offer a good combination of strong physical and chemical confinements to sulfur species for reduced sulfur loss and suppressed polysulfide shuttling. Meanwhile, the fibrous carbon skeleton strings the carbon cube fillers together to provide improved electrical contacts and excellent long-range conductivity within the whole matrix, thus enabling fast sulfur redox kinetics even under a high sulfur loading. In addition, the CNTs rooted on the carbon cube fillers not only provide additional N sites for chemical polysulfide adsorption, but also intertwine at the junctions between the adjacent fibers to strengthen the structural integrity as well as facilitate electron conduction within the entire matrix. These structural superiorities of the as-developed CPZC endow the corresponding sulfur electrodes with high sulfur utilization, fast reaction kinetics, and excellent cyclability even at a high sulfur loading and sparing electrolyte, revealing its great potential in the development of high-energy-density Li-S batteries for future practical applications. This work offers instructive material engineering for rational structural construction and improved Li-S chemistry, which can also be promisingly extended to various energy storage and conversion systems including lithium-ion batteries, supercapacitors, and electrochemical catalysis.

Conflicts of interest

There are no conflicts to declare.

Acknowledgements

The authors thank the support from the Natural Sciences and Engineering Research Council of Canada (NSERC) and the National Natural Science Foundation of China (21573083, 21706086). The authors also thank the technical support from the Canadian Centre of Electron Microscopy (CCEM) at McMaster University for the TEM characterizations.

References

- P. G. Bruce, S. A. Freunberger, L. J. Hardwick and J. M. Tarascon, *Nat. Mater.*, 2011, **11**, 19–29.
- G. R. Li, Z. W. Chen and J. Lu, *Chem*, 2018, **4**, 3–7.
- M. Wild, L. O'Neill, T. Zhang, R. Purkayastha, G. Minton, M. Marinescu and G. J. Offer, *Energy Environ. Sci.*, 2015, **8**, 3477–3494.
- A. Manthiram, Y. Z. Fu, S. H. Chung, C. X. Zu and Y. S. Su, *Chem. Rev.*, 2014, **114**, 11751–11787.
- B. Dunn, H. Kamath and J. M. Tarascon, *Science*, 2011, **334**, 928–935.
- Y. X. Yin, S. Xin, Y. G. Guo and L. J. Wan, *Angew. Chem., Int. Ed.*, 2013, **52**, 13186–13200.
- R. G. Cao, W. Xu, D. P. Lv, J. Xiao and J. G. Zhang, *Adv. Energy Mater.*, 2015, **5**, 1402273.
- N. Deng, W. Kang, Y. Liu, J. Ju, D. Wu, L. Li, B. S. Hassan and B. Cheng, *J. Power Sources*, 2016, **331**, 132–155.
- Q. Pang, X. Liang, C. Y. Kwok and L. F. Nazar, *Nat. Energy*, 2016, **1**, 16132.
- G. Li, S. Wang, Y. Zhang, M. Li, Z. Chen and J. Lu, *Adv. Mater.*, 2018, e1705590, DOI: 10.1002/adma.201705590.
- Y. Z. Liu, G. R. Li, J. Fu, Z. W. Chen and X. S. Peng, *Angew. Chem., Int. Ed.*, 2017, **56**, 6176–6180.
- Z. Yuan, H. J. Peng, J. Q. Huang, X. Y. Liu, D. W. Wang, X. B. Cheng and Q. Zhang, *Adv. Funct. Mater.*, 2014, **24**, 6105–6112.
- X. Q. Yu, H. L. Pan, Y. N. Zhou, P. Northrup, J. Xiao, S. Bak, M. Z. Liu, K. W. Nam, D. Y. Qu, J. Liu, T. P. Wu and X. Q. Yang, *Adv. Energy Mater.*, 2015, **5**, 1500072.
- Y. V. Mikhaylik and J. R. Akridge, *J. Electrochem. Soc.*, 2004, **151**, A1969–A1976.
- X. L. Wang, G. Li, J. D. Li, Y. N. Zhang, A. Wook, A. P. Yu and Z. W. Chen, *Energy Environ. Sci.*, 2016, **9**, 2533–2538.
- M. Hagen, D. Hanselmann, K. Ahlbrecht, R. Maca, D. Gerber and J. Tubke, *Adv. Energy Mater.*, 2015, **5**, 1401986.
- P. Bonnicksen, E. Nagai and J. Muldoon, *J. Electrochem. Soc.*, 2018, **165**, A6005–A6007.
- H. Hu, B. Y. Guan and X. W. Lou, *Chem*, 2016, **1**, 102–113.
- L. Han, T. W. Yu, W. Lei, W. W. Liu, K. Feng, Y. L. Ding, G. P. Jiang, P. Xu and Z. W. Chen, *J. Mater. Chem. A*, 2017, **5**, 16568–16572.
- J. S. Meng, C. J. Niu, L. H. Xu, J. T. Li, X. Liu, X. P. Wang, Y. Z. Wu, X. M. Xu, W. Y. Chen, Q. Li, Z. Z. Zhu, D. Y. Zhao and L. Q. Mai, *J. Am. Chem. Soc.*, 2017, **139**, 8212–8221.
- L. B. Avdeeva, D. I. Kochubey and S. K. Shaikhutdinov, *Appl. Catal., A*, 1999, **177**, 43–51.
- M. J. Matthews, M. A. Pimenta, G. Dresselhaus, M. S. Dresselhaus and M. Endo, *Phys. Rev. B: Condens. Matter Mater. Phys.*, 1999, **59**, R6585–R6588.
- A. C. Ferrari, J. C. Meyer, V. Scardaci, C. Casiraghi, M. Lazzeri, F. Mauri, S. Piscanec, D. Jiang, K. S. Novoselov, S. Roth and A. K. Geim, *Phys. Rev. Lett.*, 2006, **97**, 187401.
- R. Saito, M. Hofmann, G. Dresselhaus, A. Jorio and M. S. Dresselhaus, *Adv. Phys.*, 2011, **60**, 413–550.
- L. F. Chen, Y. Lu, L. Yu and X. W. Lou, *Energy Environ. Sci.*, 2017, **10**, 1777–1783.
- M. E. Birch, T. A. Ruda-Eberenz, M. Chai, R. Andrews and R. L. Hatfield, *Ann. Occup. Hyg.*, 2013, **57**, 1148–1166.
- C. H. Zhang, L. Fu, N. Liu, M. H. Liu, Y. Y. Wang and Z. F. Liu, *Adv. Mater.*, 2011, **23**, 1020–1024.
- H. B. Yang, J. W. Miao, S. F. Hung, J. Z. Chen, H. B. Tao, X. Z. Wang, L. P. Zhang, R. Chen, J. J. Gao, H. M. Chen, L. M. Dai and B. Liu, *Sci. Adv.*, 2016, **2**, 1501122.
- S.-K. Park, J.-K. Lee and Y. C. Kang, *Adv. Funct. Mater.*, 2017, **28**, 1705264.
- G. R. Li, W. Lei, D. Luo, Y. P. Deng, D. L. Wang and Z. W. Chen, *Adv. Energy Mater.*, 2018, **8**, 1702381.
- T. Z. Hou, W. T. Xu, X. Chen, H. J. Peng, J. Q. Huang and Q. Zhang, *Angew. Chem., Int. Ed.*, 2017, **56**, 8178–8182.
- Q. Pang, X. Liang, C. Y. Kwok and L. F. Nazar, *J. Electrochem. Soc.*, 2015, **162**, A2567–A2576.
- Q. Pang, D. Kundu, M. Cuisinier and L. F. Nazar, *Nat. Commun.*, 2014, **5**, 4759.
- Z. W. Seh, H. Wang, P.-C. Hsu, Q. Zhang, W. Li, G. Zheng, H. Yao and Y. Cui, *Energy Environ. Sci.*, 2014, **7**, 672–676.

- 35 W. L. Cai, G. R. Li, K. L. Zhang, G. N. Xiao, C. Wang, K. F. Ye, Z. W. Chen, Y. C. Zhu and Y. T. Qian, *Adv. Funct. Mater.*, 2018, **28**, 1704865.
- 36 C. Barchasz, F. Molton, C. Duboc, J. C. Lepretre, S. Patoux and F. Alloin, *Anal. Chem.*, 2012, **84**, 3973–3980.
- 37 Z. Yuan, H. J. Peng, T. Z. Hou, J. Q. Huang, C. M. Chen, D. W. Wang, X. B. Cheng, F. Wei and Q. Zhang, *Nano Lett.*, 2016, **16**, 519–527.
- 38 R. P. Fang, S. Y. Zhao, Z. H. Sun, W. Wang, H. M. Cheng and F. Li, *Adv. Mater.*, 2017, **29**, 1606823.
- 39 C. W. Lee, Q. Pang, S. Ha, L. Cheng, S. D. Han, K. R. Zavadil, K. G. Gallagher, L. F. Nazar and M. Balasubramanian, *ACS Cent. Sci.*, 2017, **3**, 605–613.
- 40 L. Cheng, L. A. Curtiss, K. R. Zavadil, A. A. Gewirth, Y. Y. Shao and K. G. Gallagher, *ACS Energy Lett.*, 2016, **1**, 503–509.
- 41 G. R. Li, C. Wang, W. L. Cai, Z. Lin, Z. P. Li and S. Q. Zhang, *NPG Asia Mater.*, 2016, **8**, e317.
- 42 L. X. Miao, W. K. Wang, K. G. Yuan, Y. S. Yang and A. B. Wang, *Chem. Commun.*, 2014, **50**, 13231–13234.